Atomic and microstructural origins of stored energy release in neutron-irradiated silicon carbide

D. J. Sprouster,[1,*] T. Koyanagi,[2,†] D. L. Drey,[3,‡] Y. Katoh,[2,§] and L. L. Snead[1,4,‖]

[1]*Department of Materials Science and Chemical Engineering, State University of New York, Stony Brook, New York 11794, USA*

[2]*Oak Ridge National Laboratory, Oak Ridge, Tennessee 37831, USA*

[3]*Department of Nuclear Engineering, University of Tennessee, Knoxville, Tennessee 37996, USA*

[4]*Massachusetts Institute of Technology, Cambridge, Massachusetts 02139, USA*

(Received 18 June 2021; accepted 20 September 2021; published 8 October 2021)

Here, we employ a combination of advanced synchrotron-based scattering characterization techniques to understand and unravel the atomic origins of the colossal stored energy release in neutron-irradiated silicon carbide. The quantification of the neutron irradiation-induced defects and their impact on the structure-property relationship are important for the design and safe operation of advanced fission and fusion reactors. Our experimental results show that the atomic structure in the as-irradiated samples is significantly perturbed due to a large fraction of vacancy- and interstitial-type defects that lead to complex microstructures and additional components in the x-ray diffraction and pair distribution function (PDF) results. We directly correlate the stored energy release to the recovery of the sublattices with PDF analysis, highlighting that the carbon interstitial- and vacancy-type defects contribute to stored energy more than those of silicon. We find these results to be striking and believe our discoveries to be timely and noteworthy given the technological importance of silicon carbide to the nuclear fission and fusion communities.

DOI: 10.1103/PhysRevMaterials.5.103601

I. INTRODUCTION

The production of Frenkel pairs in graphite by neutron irradiation was postulated by the Hungarian-American physicist Wigner [1]. Later, Szilard pointed out that, when these defects recombine, the defect formation energy of ∼8 eV is released [2]. These two phenomena became known as the Wigner effect and the Szilard complication, respectively. The energy released during the recovery of Frenkel pairs is the so-called Wigner energy. The potential danger of stored energy release during reactor operation was discovered early in the operation of the air-cooled graphite reactors at Windscale in the United Kingdom when Pile 2 started experiencing anomalous temperature increases later attributed to the Wigner effect. To prevent the buildup of excessive amounts of stored energy and prevent a fire upon release of that energy, the reactors were routinely thermally annealed to reduce the extent of the 200 °C release peak. A similar process occurs in silicon carbide (SiC), which is a component of TRISO-coated fuel particles in advanced reactors and is a candidate replacement cladding for Zircaloy [3]. The Wigner energy potential for SiC was investigated by Primak *et al.* [4]. Though that work concluded that the stored energy release of SiC was not significant, the neutron dose was appreciably low at only ∼0.04 displacements per atom (dpa). A recent study of high-purity chemical-vapor-deposited (CVD) SiC exposed to mixed spectrum fission neutrons, irradiated at ∼60 °C and up to 20 dpa, uncovered a significant Wigner energy [5]. At this temperature, the accumulation of lattice strain due to the irradiation-produced defects (Frenkel pairs) can exceed a critical level above which SiC becomes amorphous [6,7]. The energy release quantified from that study exceeds the specific heat of SiC, with 1390 J/g released upon annealing at 700 °C. The radiation-induced volumetric swelling under these irradiation conditions exceeded 8% before amorphization [8]. The volume changes and large stored energy were tentatively attributed to the radiation-induced defects calculated from molecular dynamics simulations [9]. By parsing the estimated defect contributions in SiC at these irradiation conditions [10,11], most (∼74%) stored energy was attributed to C-Frenkel defects, while the remainder was equally shared by Si-Frenkel defects and antisite defects. A detailed atomic and microstructural basis for the origins of the stored energy in SiC is however lacking and motivates this paper.

Determination of the microstructure and radiation-induced changes on the local atomic structure is difficult using microscopy methods due to the tedious sample preparation and complexity in obtaining real-space atomic information. X-ray scattering techniques require little to no complicated sample preparation and provide a more comprehensive and rapid means to determine the local atomic structure through the pair distribution function (PDF) [12–15]. PDF analysis allows quantification of deviations from perfect periodicity, incorporating both Bragg and diffuse scattering components [14,16–18]. It naturally follows that the PDF technique is an ideal method to study the nature of defects in disordered materials. Here, x-ray diffraction (XRD) and PDF experiments were

*david.sprouster@stonybrook.edu
†koyanagit@ornl.gov
‡ddrey@vols.utk.edu
§katohy@ornl.gov
‖lance.snead@stonybrook.edu

performed on samples of SiC irradiated to a range of neutron doses (0–20 dpa), and the samples were subsequently annealed to 700 °C to characterize the radiation damage on the short-, medium-, and long-range order. Analyses of the PDFs for the as-irradiated and as-annealed samples provide critical atomic and microstructural data. Complementary differential scanning calorimetry measurements were carried out to determine the energy stored in the samples due to defects and microstructural effects. We correlate the structural and thermodynamic data to understand the origins of the Wigner energy release in SiC.

II. MATERIALS AND METHODS

Ultrahigh-purity polycrystalline CVD SiC samples were acquired from Rohm & Haas Advanced Materials (presently PremaTech ADVANCED CERAMICS). The nominal purity was >99.999%. The unirradiated specimens were 6 × 6 × 2.8 mm in size. Neutron irradiation was carried out in the mixed neutron spectrum hydraulic tube or peripheral target tube positions of the High Flux Isotope Reactor (HFIR). The irradiation capsule was an aluminum tube with perforated walls through which HFIR coolant water passed and contacted the sample holders. The irradiation temperature was expected to be close to the coolant temperature, nominally ∼60 °C. Samples were irradiated to nominal neutron doses of 0.02×10^{25}, 0.1×10^{25}, 0.5×10^{25}, 2.0×10^{25}, and 20×10^{25} n/m^2 ($E > 0.1$ MeV). The fast neutron flux at this position of HFIR was $\sim 1 \times 10^{19}$ n m^{-2} s^{-1} ($E > 0.1$ MeV) corresponding to $\sim 10^{-6}$ dpa/s. The fluence was calculated based on the known flux in the irradiation position and the elapsed irradiation time. It was considered accurate within a few percent. In this paper, a fluence of 1×10^{25} n/m^2 ($E > 0.1$ MeV) was assumed to be equivalent to a dose of 1 dpa. The nominal fluence was calculated based on calculations using the HFIR neutron spectrum and an assumed displacement energy of 30 eV [19], and the predominate damage mode was through nuclear stopping.

Calorimetric measurements were carried out for the specimens cleaned with hydrofluoric acid using a Netzsch DSC 404C Thermal Analyzer to determine the stored energy. The heating rate was set to be 20 °C/min and the maximum temperature reached was 700 °C. Details of the stored energy measurements can be found elsewhere [5]. XRD and x-ray total scattering measurements were performed at the National Synchrotron Light Source II (NSLS-II) at Brookhaven National Laboratory (BNL) using the x-ray powder diffraction (XPD) beamline 28-ID-2 [20,21]. All measurements were performed in transmission mode. The sample-to-detector distance and tilts of the detector relative to the beam were refined using a LaB_6 National Institute of Standards and Technology powder standard. The wavelength of the incident x rays was 0.1877 Å (66.05 keV), and the sample-to-detector distances were calculated to be 1567.99 mm (for XRD) and 199.16 mm (for PDF). The samples were wrapped in Kapton tape to limit radioactive contamination during shipping and handling at the beamline, and samples were continuously rotated in the plane perpendicular to the beam (XY) during acquisition to improve powder averaging. The two-dimensional detector images were radially integrated to obtain one-dimensional powder diffraction patterns. The background Kapton containment and air scattering components were subtracted from the individual XRD patterns.

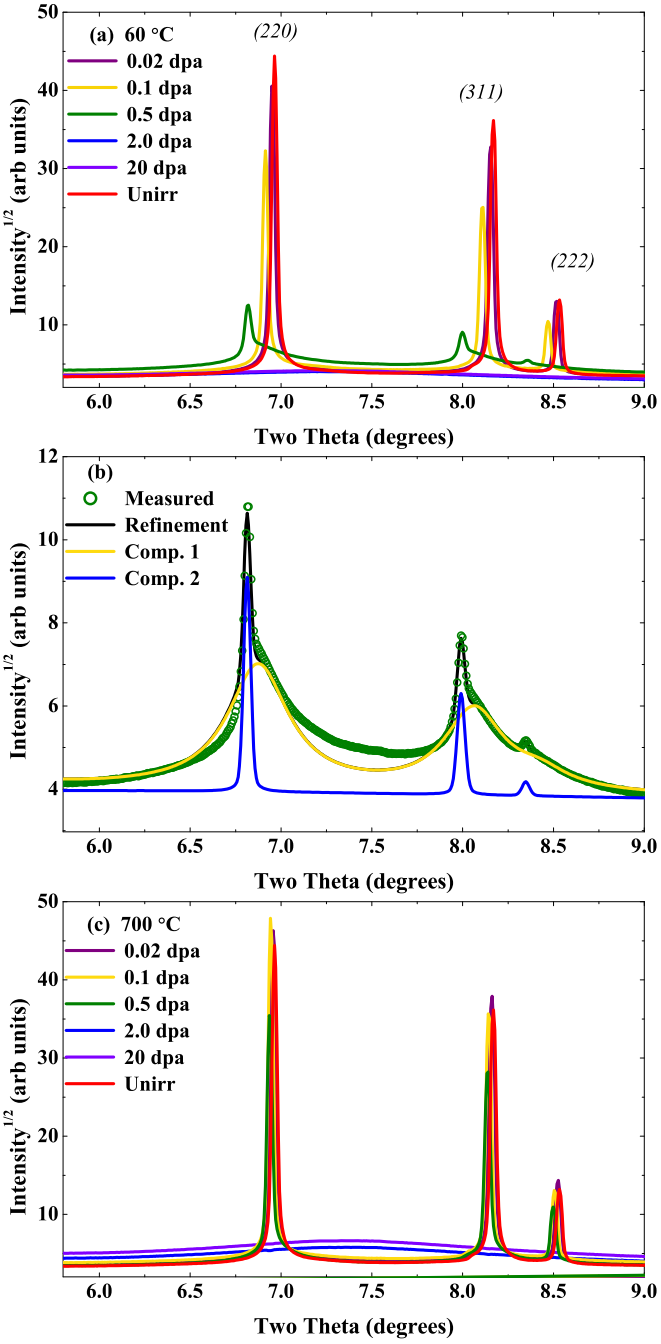

FIG. 1. X-ray diffraction (XRD) patterns around the (220), (311), and (222) peaks for (a) SiC specimens as irradiated nominally at 60 °C, (b) the Rietveld refinement for the 0.5 dpa specimen with two refined SiC components, and (c) XRD patterns of the SiC specimens annealed at 700 °C.

Rietveld refinements were performed on the corrected XRD patterns to determine the lattice parameter. The peak profiles for the SiC reflections were modeled using a modified pseudo-Voigt function in MAUD [22]. The instrument contribution to the broadening of the measured profiles was quantified by fitting a LaB_6 standard with known crystalline domain size and negligible strain contribution. The instrument-based

TABLE I. Quantitative XRD results from Rietveld refinements. The rows with an asterisk are the results for the additional SiC component observed in the XRD. Stored energy values are from Ref. [5].

Neutron dose (dpa)	Annealing conditions	Unit cell parameter (Å)	Coherent grain size (nm)	Microstrain ($\times 10^{-5}$)	Weight fraction (%)	Stored energy (J/gm)
0	–	4.37019 (0.00003)	175.3 (3.1)	1.45 (0.8)	100	–
0.02	–	4.37895 (0.00003)	158.8 (2.1)	17.5 (1.0)	100	150
0.02	Up to 700 °C	4.37454 (0.00004)	174.8 (3.2)	7.5 (0.8)	100	–
0.1	–	4.40244 (0.00004)	155.0 (5.4)	25.0 (5.0)	87.9 (0.5)	480
0.1*	–	4.36635 (0.00885)	2.8 (1.0)	–	12.1 (0.5)	–
0.1	Up to 700 °C	4.38376 (0.00004)	142.1 (5.8)	9.7 (1.0)	100	–
0.5	–	4.46218 (0.00013)	105 (5.1)	164.4 (2.6)	40.4 (0.6)	1500
0.5*	–	4.40524 (0.00115)	3.1 (1.0)	–	59.6 (0.4)	–
0.5	Up to 700 °C	4.38737 (0.00006)	130.6 (5.9)	32.0 (10.0)	100	–

broadening parameters were subsequently fixed during the analysis of the SiC specimens. The lattice parameter, microstrain, and coherent grain size components were allowed to vary during the Rietveld refinements. The diffraction patterns from the shorter sample-to-detector distance were corrected for PDF-specific corrections (self-absorption, multiple scattering, and Compton scattering) and converted to atomic PDFs $G(r)$ using PDFGETX3 over a Q-range of 0.1–24 $Å^{-1}$. The PDF structural analysis was carried out using PDFGUI [23] over a radial range of 1.0–50 Å. A Ni standard was used to determine the parameters that describe the experimental resolution (Q_{damp} and Q_{broad}) with atomic displacement parameters (ADPs), correlated motion parameter, and lattice parameters allowed to vary. The ADPs capture diminished x-ray intensity from atom displacements from their mean positions in a crystal structure and can include components from both temperature-dependent atomic vibrations (thermal disorder) and static disorder (such as defects). The scale factor, lattice parameters, correlated motion parameter, and anisotropic ADPs were allowed to refine during the PDF analysis for all specimens (using an $F\bar{4}3m$ zinc blende crystal phase). The $F\bar{4}3m$ crystal structure consists of two intersecting face-centered cubic sublattices, with Si atoms located on the 4*a* Wyckoff equipoint with coordinates (0, 0, 0), C atoms on the 4*c* equipoint with coordinates ($\frac{1}{4}$, $\frac{1}{4}$, $\frac{1}{4}$), and a lattice parameter of 4.36 Å. To quantify the short-range structure in the 0.1 and 0.5 dpa as-irradiated specimens, an additional component was included to capture the interstitial defects.

III. RESULTS AND DISCUSSION

The XRD patterns for the as-irradiated and annealed specimens are shown in Fig. 1. With increasing neutron dose, the Bragg peaks decrease in height and substantially increase in width, indicating that the coherent grain size (that is, the size of the defect-free material within a grain) decreases [Fig. 1(a)]. Peak shifts to lower 2θ angles, as highlighted in Fig. 1(a), are due to the expansion of the unit cell from the incorporation of point defects and defect clusters into the crystal structure; this trend is consistent with past works [12,24]. The expanded regions around the (220), (311), and (222) diffraction peaks for the 0.1 and 0.5 dpa specimens show significant diffuse peaks that mark the appearance of an additional component at higher 2θ angles [Fig. 1(b)]. This additional diffraction component has a structure akin to the strained host ($F\bar{4}3m$), albeit with reduced coherent grain size and smaller unit cell parameters. The XRD patterns for the 2.0 and 20 dpa specimens show no sharp features and only broad, highly diffuse peaks, indicating total loss of crystallinity. Upon annealing, the microstructure of the 0.02–0.5 dpa samples recover, with an increase in peak height and decrease in peak width (relative to the as-irradiated specimen) [Fig. 1(c)]. The Bragg peaks shift toward the original higher 2θ positions of the pristine specimen, indicating recovery of the unit cell parameter. The diffuse components observed in the 0.1 and 0.5 dpa as-irradiated specimens are completely removed after annealing, while the 2.0 and 20 dpa specimens remain amorphous, and only subtle changes in the height of the amorphous peaks are observed. Interestingly, the 0.1 and 0.5 dpa specimens do not show full recovery of peak intensity and position after annealing at 700 °C, indicating either the annealing time was too short for full recovery of the crystal structure (samples heated at 700 °C for 20 min), or a portion of the defects present at this damage level cannot be removed with these annealing conditions.

Rietveld refinement was performed on all as-irradiated and as-annealed specimens; results are listed in Table I. The unit cell and microstructural trends described previously are quantitatively confirmed by the refinements, and the lattice expansions quantified from the Rietveld analysis in the as-irradiated specimens are in agreement with previous XRD analyses of neutron irradiated SiC [5,8]. Including the second SiC component in the refinements for the 0.1 and 0.5 dpa as-irradiated patterns was necessary to effectively capture the additional diffuse intensity on the high 2θ side of the Bragg peaks. Quantitative microstructural analysis confirms that, postirradiation, the SiC specimens are significantly perturbed relative to the unirradiated state. At the highest fluence before amorphization, the coherent grain sizes of the SiC specimens decrease by ∼40%, while the microstrain grows by ∼2 orders of magnitude. The second SiC component comes from the large defect populations introduced during the irradiation, leading to a reduced amount of defect-free coherent volume (as described below). The large defect populations also lead to the increase in the microstrain and smaller coherent grain sizes. Similar XRD signatures have been observed in other

highly irradiated ceramic materials [25–27]. The microstructural recovery from the postirradiation annealing includes a decrease in the microstrain, increase in coherent grain size, and removal of the second SiC component. Subtle differences in the final annealed microstrain, grain size, and lattice parameters compared with the nonirradiated specimen show that the postirradiation annealing has not removed all defects, and minor populations of extended defects (dislocations) and atomistic defects (antisite defects) may still be present, though the amount and type of defects retained cannot be confirmed in this paper and should be further investigated in future studies.

The standard XRD and Rietveld refinements can only reveal and model structural features that are apparent in the long-range, repeating crystal structure. Complementary x-ray total scattering was performed on the as-irradiated and as-annealed SiC specimens to probe the local atomic configuration and to observe defects that do not directly contribute to the Bragg scattering observed using XRD. Total scattering experiments recording the scattering of x rays at both low and very high scattering angles give information on both the Bragg peaks as well as the diffuse scattering between the Bragg peaks and at high scattering angles which correspond to very small d spacings. The PDF $G(r)$ is produced from these comprehensive scattering data and is a real-space representation of the nearest neighbor atomic correlations, allowing analysis of local atomic configurations (and thus short-range order). The high-r correlations ($r > 15$ Å, not shown), which exist at high enough radial distances to approximate the long-range structure, show a decrease in peak intensity and a shift of peaks to higher r values with increasing neutron dose. This behavior corroborates the increasing defect levels and expanding unit cells determined previously using XRD. At 2.0 dpa and higher, there are no correlations in this r range which indicate complete amorphization, as determined in previous work [28].

The short-range structure is shown at low r ($r < 12$ Å) and contains the nearest neighbor pairwise correlations [Fig. 2(a)]. For example, the nearest neighbor tetrahedral Si-C bonds are represented by the peak at $r = 1.9$ Å, while the peak at 3.1 Å contains the first nearest neighbor C-C and Si-Si correlations. This region shows systematic decreases in correlation peak heights and increases in peak width with dose. The PDF peak areas give information on coordination numbers and peak widths on thermal vibrations and structural disorder. The reduction of peak intensities and increase in peak broadening (and loss of some correlation peaks) is caused here by an increase in structural disorder and the accumulation of substantial point defects and defect clusters. The fine structure in the amorphous specimens, specifically the heteronuclear (Si-C) bonds and homonuclear (Si-Si and C-C) bonds, are consistent with past studies in irradiated SiC [29,30] and other compound semiconductors [31].

Figure 2(b) shows an example of the PDF refinements for the 0.5 dpa specimen with and without the inclusion of the interstitial component (described below). The inclusion of the interstitial component leads to an improved refinement of the intensity under the correlation peaks in the short range (up to ∼15 Å) and lower residuals (shown in green). After annealing, the PDFs show that both short- and medium-range

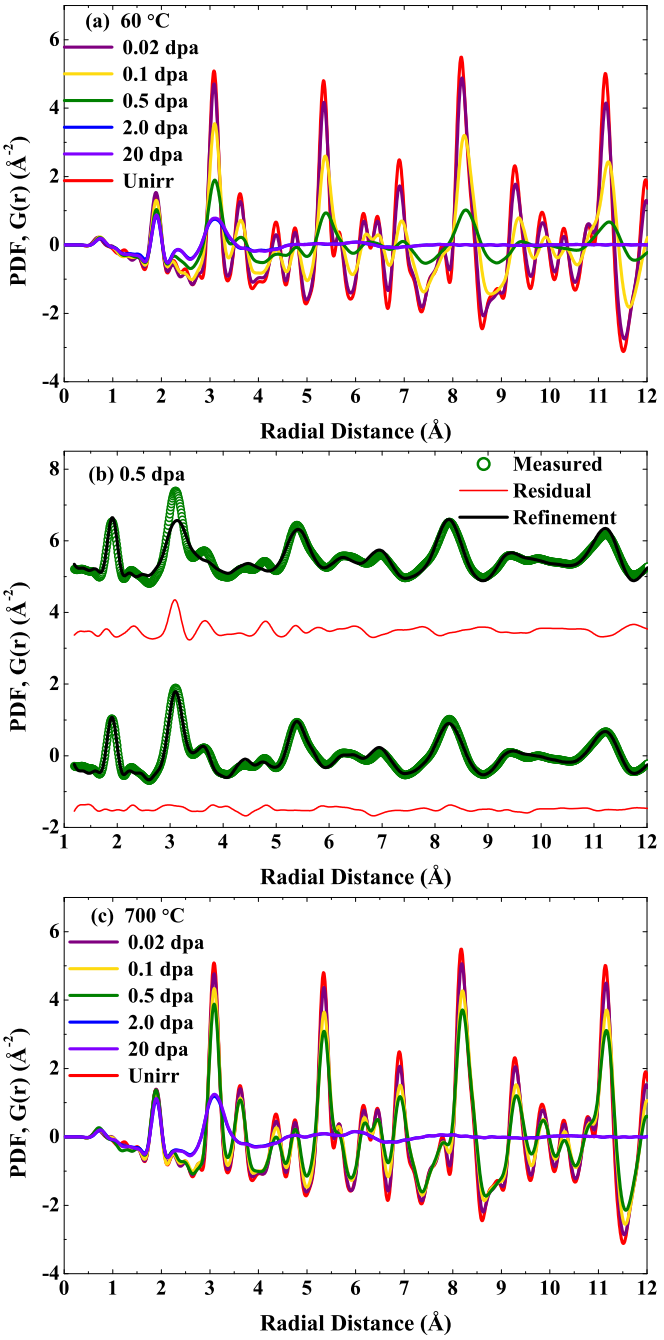

FIG. 2. Pair distribution function (PDFs) of (a) as-irradiated, (b) example of the PDF refinement for the 0.5 dpa specimen with and without the second nanophase (green is residual from refinement), and (c) as-annealed SiC specimens.

orders recover for the 0.02–0.5 dpa specimens [Fig. 2(c)]. This is evidenced by an increase in peak correlation heights and reduction in correlation widths. This structural repair is like the XRD results shown in Fig. 1(c). The PDFs do show that some residual structural disorder remains after annealing (decreased correlation peak heights relative to unirradiated specimen). Although the 2.0 and 20 dpa samples remain amorphous after annealing, subtle changes in the short-range order, including a reduction in the homonuclear bonding (Si-Si and C-C bonds), decrease with annealing (relaxed amorphous structure), again

TABLE II. Quantitative PDF results from small-box refinements in the fit range of $r = 1.2$–50 and 1.2–15 Å. The rows with an asterisk are the results for the nanocrystalline component. R_w is the weighted residual of the refinements.

Neutron dose (dpa)	0	0.02	0.02 (700 °C)	0.1	0.1 (700 °C)	0.5	0.5 (700 °C)
$r = 1.2$–50							
R_w	0.15	0.15	0.13	0.18	0.15	0.32	0.15
Unit cell parameter (Å)	4.362 (0.001)	4.366 (0.014)	4.369 (0.012)	4.392 (0.002)	4.374 (0.002)	4.430 (0.005)	4.373 (0.001)
4*a* (Si) ADP (Å^2)	0.0040 (0.0001)	0.0048 (0.0002)	0.0047 (0.0003)	0.0087 (0.0005)	0.0055 (0.0004)	0.0303 (0.004)	0.0071 (0.0003)
4*c* (C) ADP (Å^2)	0.0055 (0.0004)	0.0065 (0.0006)	0.0067 (0.0008)	0.0158 (0.0021)	0.0078 (0.0009)	0.0787 (0.030)	0.0105 (0.0012)
$r = 1.2$–15 Å							
R_w	0.12	0.14	0.13	0.16	0.15	0.14	0.15
Unit cell parameter (Å)	4.362 (0.001)	4.365 (0.014)	4.369 (0.001)	4.394 (0.003)	4.373 (0.002)	4.417 (0.012)	4.372 (0.002)
4*a* (Si) ADP (Å^2)	0.0042 (0.002)	0.0052 (0.0003)	0.0048 (0.0003)	0.0102 (0.001)	0.0061 (0.0004)	0.0265 (0.0063)	0.0076 (0.0005)
4*c* (C) ADP (Å^2)	0.0058 (0.006)	0.0066 (0.0009)	0.0067 (0.0008)	0.0196 (0.006)	0.0085 (0.0011)	0.0543 (0.033)	0.0109 (0.0016)
Unit cell parameter (Å)*	–	–	–	4.3788 (0.015)	–	4.389 (0.029)	–
4*a* (Si) ADP (Å^2)*	–	–	–	0.0021 (0.0010)	–	0.0085 (0.0055)	–
4*c* (C) occupancy*	–	–	–	1 (fixed)	–	0.6303 (0.3)	–
4*c* (C) ADP (Å^2)*	–	–	–	0.0039 (0.0010)	–	0.0054 (0.0014)	–
24*f* (C) ADP (Å^2)*	–	–	–	–	–	0.0164 (0.01)	–
24*f* (C) *x*-position*	–	–	–	–	–	0.3116 (0.084)	–
Atom fraction*	–	–	–	0.37 (0.03)	–	0.57 (0.11)	–
Coherent length (Å)*	–	–	–	12.9 (3.8)	–	9.2 (2.5)	–

consistent with previous studies of amorphous SiC [32]. We note that the physical properties of neutron-irradiated SiC (density, electrical resistivity, thermal conductivity) also continually change with postirradiation annealing (in the absence of crystallization) and are attributed to changes in the short- and medium-range ordering [30]. Future *in situ* experiments employing PDF could be leveraged to quantify the roles of short- and medium-range order on the physical property recovery.

The long-range structural models determined using XRD were used as initial starting parameters in the small-box PDF modeling of the 0, 0.02, 0.1, and 0.5 dpa specimens for $r = 1.2$–50 Å (Table II) to determine how well the long-range structure reproduces the PDFs. The 3C-SiC $F\bar{4}3m$ model fits the PDFs of the 0, 0.02, and 0.1 dpa specimens well with no unphysical structures or highly correlated parameters. The goodness-of-fit parameter R_w increases with increasing dose, indicating an increasing mismatch between the average and local structure. The small-box fit of the 0.5 dpa PDF resulted in a high R_w value of 0.32, with the low-r region ($r < 12$ Å) being poorly refined with this simple model. There is a general upward trend of the unit cell parameters and ADPs, in agreement with the XRD results, indicating accumulation of defects in the crystal. The unit cell parameters are smaller than those determined from XRD due to the explicit modeling of the distortions induced by the local defect structure as separate from the regular crystal. When analyzing the Bragg scattering (XRD), these distortions are not explicitly observable and are instead averaged with the regular crystal, resulting in a perceived increase in the microstrain, atomic thermal parameters, and unit cell parameter. Upon annealing at 700 °C, the PDFs of all specimens show recovery with parameters returning to near-pristine levels; the level of recovery is reduced with increasing dose, consistent with the XRD results above.

To better understand the local atomic environment and separate the correlations related to the highly defective crystal regions from the average crystal structure, small-box refinement was performed on the PDFs from 1.2 to 15 Å, a window that includes the entirety of the defective crystal extent determined in the full PDF refinements while excluding average phase correlations outside the defect region coherent length (Table I). For the 0, 0.02, 0.1, and 0.5 dpa specimens, the PDF was fit well ($R_w < 0.16$) with the regular 3C-SiC $F\bar{4}3m$ model and the inclusion of a secondary component for the 0.1 and 0.5 dpa samples [0.5 dpa refinements are shown in Fig. 2(b) for reference]. No secondary phase was detected in the PDFs of the pristine and 0.02 dpa specimens, though increases in the ADPs indicate increasing defect populations and disorder. The secondary phases were modeled with a modified nanocrystalline $F\bar{4}3m$ structure where carbon atoms were allowed to occupy the octahedral interstitial position [Fig. 3(a)] through movement of carbon from their normal sites, essentially modeling a carbon Frenkel pair. Multiple atomic sites within the silicon octahedron were tested to determine the best approach to modeling carbon interstitials. A single position at the 4*b* site (0.5, 0.5, 0.5) was fit to model a centrally located carbon interstitial [Fig. 3(b)]. This approach did not capture the pair correlations at ∼2.3 Å, which includes Si-C and C-C pair correlations between regular lattice atoms and carbon interstitials [29] and resulted in the carbon interstitial having negative ADPs of high magnitude, indicating the carbon interstitial lies too far from the surrounding silicon and carbon atoms. Carbon interstitials are known to distort from the center of the silicon octahedra, close to two 16*e* sites $(\frac{1}{3}, \frac{1}{3}, \frac{1}{3})$ and $(\frac{2}{3}, \frac{2}{3}, \frac{2}{3})$ [Fig. 3(c)], to maintain bonding to four other atoms [33,34]. Despite being located at more physically accurate positions, modeling the 16*e* sites resulted in unphysical ADPs since this configuration places carbon atoms very close to other carbon

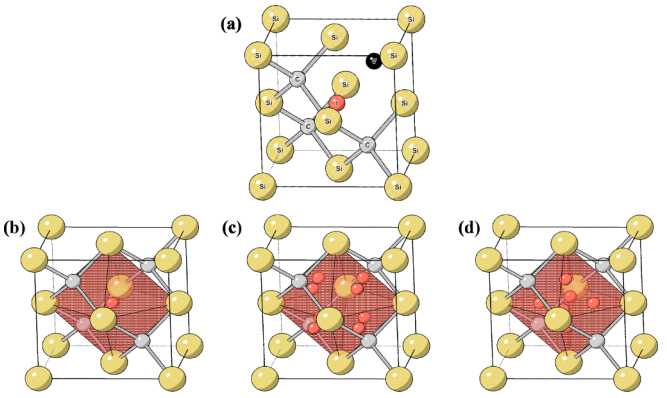

FIG. 3. (a) Carbon Frenkel pair in 3C-SiC where the carbon interstitial sits on the 4*b* Wyckoff equipoint octahedral site. Silicon is gold spheres, carbon is gray spheres, and the interstitial and vacancy are represented by red and black spheres, respectively. Silicon octahedron with (b) carbon interstitial at the center 4*b* site, (c) with carbon interstitials in the octahedron faces at 16*e* sites along ⟨111⟩ directions, and (d) with carbon interstitials at 24*f* sites along ⟨100⟩ directions.

atoms in the occupied 4*c* site and does not fully capture the pair correlations represented by the peak at ∼2.3 Å. Placing the carbon interstitials at the 24*f* site [Fig. 3(d)], which is located at (x, 0.5, 0.5), resulted in the best fit to the data and the most physically reasonable structure. Using the 24*f* site configuration approximates the pair correlations produced by carbon Frenkel pairs while avoiding the underbonding and overbonding produced by the two previous models. The x position of this site gives information on the average distortion of the carbon interstitial from the center of the silicon cage and changes the position and shape of the peak at ∼2.3 Å. For the 24*f* site, a value of $x = 0.5$ places the interstitial at the center of the silicon octahedral cage; decreasing the x position shifts the carbon along ⟨100⟩ directions and closer to the surrounding silicon and carbon atoms. In the 0.1 dpa sample, defects are extensive enough that a second distorted phase could be extracted but not in a high enough concentration that carbon interstitials could be refined within this phase. In contrast, a significant amount of carbon Frenkel pairs can be fitted to the PDF of the 0.5 dpa specimen. The refined x position value of $\sim \frac{1}{3}$ is evidence that the carbon interstitial is highly distorted from the center of the silicon octahedral cage [33,34]. The amount of nanocrystalline phase is extensive at this high dose level (57 at.%), and the interstitial 24*f* positions are ∼6% occupied, which equates to ∼1.48 carbon interstitials per unit cell. More than one interstitial per unit cell indicates that interstitial clustering may be occurring at the 0.5 dpa dose level. Other configurations that included silicon interstitials and antisite defects were tested but did not result in satisfactory fits to the data. It is likely these types of defects are too low in concentration for PDF small-box refinements to directly model but are high enough in concentration to impact the ADPs.

The recovery of irradiation-induced defects in SiC accompanies recovery of the lattice swelling (see Table I). As the bond lengths change, the cohesive energy also changes, which could be a source of stored energy release. An estimation of

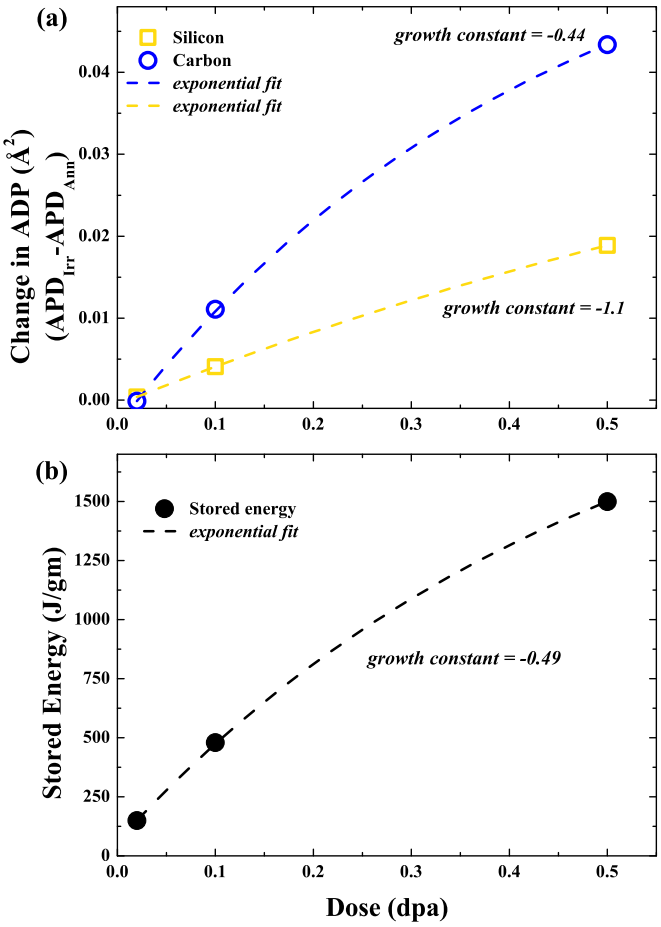

FIG. 4. (a) Si and C sublattice atomic displacement parameters (ADPs) determined from the pair distribution function (PDF) refinements for the as-irradiated and as-annealed specimens. (b) The stored energy measured as a function of dose. Lines in (a) and (b) are exponential fits to the data.

the influence of lattice relaxation on stored energy release was attempted using the Tersoff potential [35]. The calculated changes in the cohesive energy are 4.5×10^{-5}, 8.5×10^{-3}, and 2.7×10^{-2} eV per bond for the 0.02, 0.1, and 0.5 dpa specimens, respectively, which corresponds to stored energy changes of 0.4, 82, and 260 J/g, respectively. The lattice recovery contributed to only <20% of the stored energy release shown in Ref. [5]. Therefore, it is expected that recombination of the Frenkel pairs is a major source of the energy release. The ADPs quantitively determined from the PDF analysis are a direct measure of the structural disorder present within the material [36–39] and can be used to track the amount of disorder on both the carbon and silicon sublattices [12]. Deviations in their values are indications that the local structure is different and, in the case described here, are sensitive to the number of vacancies, slight static deviations from lattice sites, and antisite defects. Both ADPs for the silicon and carbon sublattices systematically increase with increasing dose and, therefore, with increasing levels of defects. The ADPs for the carbon sublattice are much larger than those for the silicon sublattice, indicating that the carbon sublattice is more disordered. This agrees with past works that show that the

carbon sublattice shows a higher vacancy concentration after irradiation damage; indeed, calculations show that silicon defects are more energetically costly and make up a smaller fraction of the total defect population (Snead *et al.* [5]). The stored energy and the recovery of the carbon sublattice have near identical exponential behavior (Fig. 4). The recovery of the ADPs for the silicon and carbon sublattices, as determined from the PDF refinements, highlight that the recombination of carbon defects is more dominant than silicon defects during annealing.

IV. CONCLUSIONS

In summary, we have performed detailed XRD and PDF analyses of neutron-irradiated SiC to quantify the atomic and microstructural properties of as-irradiated and as-annealed specimens with doses before the onset of the amorphization. The XRD and PDF results show that the atomic structure in the as-irradiated samples is significantly perturbed due to a large fraction of vacancies and interstitial-type defects. The large defect populations introduced by neutron irradiation include point defects which increase in concentration with increasing dose level, leading to the expanded lattice parameters and large ADPs. These defects reduce the coherent volume by shortening the width of the unperturbed crystal regions and drive the emergence of additional diffraction/scattering components with small coherent volumes. Subsequent annealing leads to the removal of a large fraction of these point defects and the formation of some extended defects which manifest as larger microstrain values and smaller coherent grain sizes than the unirradiated state. The analysis of the PDF data, incorporating a disordered component with carbon interstitials at $24f$ sites along $\langle 100 \rangle$ directions, captures the additional correlation peaks visible in the high-dose specimens. The ADPs quantified from the PDF analysis demonstrate that the primary defects associated with damaged SiC are carbon vacancies and interstitials and that recovery of the microstructure and different sublattices is highly correlated to the stored energy release, consistent with the initial postulation that the stored energy release in SiC is dominated by the recovery of carbon-based defects. The combination of XRD and PDF represents a strategy to determine the full spectrum of atomic and microstructural defects present in neutron-irradiated materials and has the potential to validate simulations of radiation damage in other materials of interest. Finally, the impact of this paper has broad implications in generating structure-property relationships in neutron-irradiated materials where generating connections between the atomistic and defect structures can aid in understanding changes in macroscopic properties of interest.

ACKNOWLEDGMENTS

These experiments and analyses were supported by the U.S. Department of Energy (DOE) Office of Fusion Energy Sciences under Contract No. DE-SC0018322 with the Research Foundation for the State University of New York at Stony Brook and No. DE-AC05-00OR22725 with UT-Battelle, LLC. This paper was supported by the DOE, Office of Nuclear Energy under DOE Idaho Operations Office Contract No. DE-AC07-051D14517 as part of a Nuclear Science User Facilities experiment. Use of the National Synchrotron Light Source-II, Brookhaven National Laboratory, was supported by the DOE under Contract No. DE-SC0012704. The irradiation experiment was supported by DOE Office of Nuclear Energy, Advanced Fuel Campaign under Contract No. DE-AC05-00OR22725 with Oak Ridge National Laboratory (ORNL), managed by UT-Battelle, LLC. A portion of this research used resources at the HFIR, a DOE Office of Science User Facility operated by ORNL.

[1] E. Wigner, *Report for Month Ending December 15, Physics Division* (US Atomic Energy Commission Report CP-387, Univ. of Chicago, Chicago, 1942).

[2] J. H. W. Simmons, *Radiation Damage in Graphite* (Pergamon, London, 1965).

[3] Y. Katoh and L. L. Snead, Silicon carbide and its composites for nuclear applications—historical overview, J. Nucl. Mater. **526**, 151849 (2019).

[4] W. Primak, L. H. Fuchs, and P. P. Day, Radiation damage in diamond and silicon carbide, Phys. Rev. **103**, 1184 (1956).

[5] L. L. Snead, Y. Katoh, T. Koyanagi, and K. Terrani, Stored energy release in neutron irradiated silicon carbide, J. Nucl. Mater. **514**, 181 (2019).

[6] L. L. Snead, T. Nozawa, Y. Katoh, T. S. Byun, S. Kondo, and D. A. Petti, Handbook of SiC properties for fuel performance modeling, J. Nucl. Mater. **371**, 329 (2007).

[7] L. L. Snead, S. J. Zinkle, J. C. Hay, and M. C. Osborne, Amorphization of SiC under ion and neutron irradiation, Nucl. Instrum. Methods Phys. Res. B **141**, 123 (1998).

[8] L. L. Snead, Y. Katoh, T. Koyanagi, K. Terrani, and E. D. Specht, Dimensional isotropy of 6H and 3C SiC under neutron irradiation, J. Nucl. Mater. **471**, 92 (2016).

[9] J. Li, L. Porter, and S. Yip, Atomistic modeling of finite-temperature properties of crystalline β-SiC: II. Thermal conductivity and effects of point defects, J. Nucl. Mater. **255**, 139 (1998).

[10] F. Gao and W. J. Weber, Cascade overlap and amorphization in 3C-SiC: defect accumulation, topological features, and disordering, Phys. Rev. B **66**, 024106 (2002).

[11] N. Swaminathan, D. Morgan, and I. Szlufarska, *Ab initio* based rate theory model of radiation induced amorphization in β-SiC, J. Nucl. Mater. **414**, 431 (2011).

[12] D. J. Sprouster, L. L. Snead, E. Dooryhee, S. K. Ghose, T. Koyanagi, and Y. Katoh, Pair distribution function analysis of neutron-irradiated silicon carbide, J. Nucl. Mater. **527**, 151798 (2019).

[13] D. J. Sprouster, J. R. Trelewicz, L. L. Snead, X. Hu, D. Morrall, T. Koyanagi, C. M. Parish, L. Tan, Y. Katoh, and B. D. Wirth, Advanced synchrotron characterization techniques for fusion materials science, J. Nucl. Mater. **543**, 152574 (2021).

[14] D. L. Drey, E. C. O'Quinn, T. Subramani, K. Lilova, G. Baldinozzi, I. M. Gussev, A. F. Fuentes, J. C. Neuefeind, M. Everett, D. Sprouster, A. Navrotsky, R. C. Ewing, and M. Lang,

Disorder in $Ho_2Ti_{2-x}Zr_xO_7$: pyrochlore to defect fluorite solid solution series, RSC Adv. **10**, 34632 (2020).

[15] E. C. O'Quinn, K. E. Sickafus, R. C. Ewing, G. Baldinozzi, J. C. Neuefeind, M. G. Tucker, A. F. Fuentes, D. Drey, and M. K. Lang, Predicting short-range order and correlated phenomena in disordered crystalline materials, Sci. Adv. **6**, eabc2758 (2020).

[16] T. Proffen, S. Billinge, T. Egami, and D. Louca, Structural analysis of complex materials using the atomic pair distribution function—a practical guide, Z. Kristallogr. **218**, 132 (2003).

[17] D. A. Keen and A. L. Goodwin, The crystallography of correlated disorder, Nature (London) **521**, 303 (2015).

[18] M. Zhao, E. O'Quinn, N. Birkner, Y. Xu, M. Lang, and K. Brinkman, Radiation damage and thermal annealing in tunnel structured hollandite materials, Acta Mater. **206**, 116598 (2021).

[19] G. Newsome, L. L. Snead, T. Hinoki, Y. Katoh, and D. Peters, Evaluation of neutron irradiated silicon carbide and silicon carbide composites, J. Nucl. Mater. **371**, 76 (2007).

[20] X. Shi, S. Ghose, and E. Dooryhee, Performance calculations of the x-ray powder diffraction beamline at NSLS-II, J. Synchrot. Radiat. **20**, 234 (2013).

[21] D. J. Sprouster, R. Weidner, S. K. Ghose, E. Dooryhee, T. J. Novakowski, T. Stan, P. Wells, N. Almirall, G. R. Odette, and L. E. Ecker, Infrastructure development for radioactive materials at the NSLS-II, Nucl. Instrum. Methods Phys. Res. A **880**, 40 (2018).

[22] L. Lutterotti, S. Matthies, H.-R. Wenk, A. S. Schultz, and J. W. Richardson, Combined texture and structure analysis of deformed limestone from time-of-flight neutron diffraction spectra, J. Appl. Phys. **81**, 594 (1997).

[23] C. Farrow, P. Juhas, J. Liu, D. Bryndin, E. Božin, J. Bloch, T. Proffen, and S. Billinge, PDFFIT2 and PDFGUI: computer programs for studying nanostructure in crystals, J. Phys. Condens. Mater. **19**, 335219 (2007).

[24] D. J. Sprouster, T. Koyanagi, E. Dooryhee, S. K. Ghose, Y. Katoh, and L. E. Ecker, Microstructural evolution of neutron irradiated 3C-SiC, Scripta Mater. **137**, 132 (2017).

[25] N. Simos, P. Hurh, E. Dooryhee, L. Snead, D. Sprouster, Z. Zhong, H. Zhong, S. Ghose, Z. Kotsina, K. Ammigan, J. Hylen, V. Papadimitriou, R. Zwaska, D. Senor, A. Casella, and D. J. Edwards, 120 GeV neutrino physics graphite target damage assessment using electron microscopy and high-energy x-ray diffraction, Phys. Rev. Accel. Beams. **22**, 041001 (2019).

[26] N. Simos, P. Hurh, N. Mokhov, M. Snead, M. Topsakal, M. Palmer, S. Ghose, H. Zhong, Z. Kotsina, and D. J. Sprouster, Low-temperature proton irradiation damage of isotropic nuclear grade IG-430 graphite, J. Nucl. Mater. **542**, 152438 (2020).

[27] N. Simos, E. Quaranta, N. Charitonidis, D. Sprouster, Z. Zhong, S. Ghose, Z. Kotsina, R. Assmann, S. Redaelli, A. Bertarelli, and A. I. Ryazanov, Radiation damage of a two-dimensional carbon fiber composite (CFC), Carbon Trends **3**, 100028 (2021).

[28] L. L. Snead and J. C. Hay, Neutron irradiation induced amorphization of silicon carbide, J. Nucl. Mater. **273**, 213 (1999).

[29] M. Ishimaru, I. T. Bae, Y. Hirotsu, S. Matsumura, and K. E. Sickafus, Structural Relaxation of Amorphous Silicon Carbide, Phys. Rev. Lett. **89**, 055502 (2002).

[30] L. Snead and S. Zinkle, Structural relaxation in amorphous silicon carbide, Nucl. Instrum. Methods Phys. Res. B **191**, 497 (2002).

[31] C. S. Schnohr and M. C. Ridgway, *X-ray Absorption Spectroscopy of Semiconductors* (Springer, Berlin, Heidelberg, 2015).

[32] M. Ishimaru, A. Hirata, M. Naito, I. T. Bae, Y. W. Zhang, and W. J. Weber, Direct observations of thermally induced structural changes in amorphous silicon carbide, J. Appl. Phys. **104**, 033503 (2008).

[33] C. Jiang, D. Morgan, and I. Szlufarska, Structures and stabilities of small carbon interstitial clusters in cubic silicon carbide, Acta Mater. **62**, 162 (2014).

[34] C. Jiang, D. Morgan, and I. Szlufarska, Carbon tri-interstitial defect: a model for the DII center, Phys. Rev. B **86**, 144118 (2012).

[35] J. Tersoff, Modeling solid-state chemistry: interatomic potentials for multicomponent systems, Phys. Rev. B **39**, 5566 (1989).

[36] T. Egami and S. J. Billinge, *Underneath the Bragg Peaks: Structural Analysis of Complex Materials* (Elsevier, Oxford, England, 2003).

[37] M. Lang, C. L. Tracy, R. I. Palomares, F. Zhang, D. Severin, M. Bender, C. Trautmann, C. Park, V. B. Prakapenka, V. A. Skuratov, and R. C. Ewing, Characterization of ion-induced radiation effects in nuclear materials using synchrotron x-ray techniques, J. Mater. Res. **30**, 1366 (2015).

[38] R. I. Palomares, M. T. McDonnell, L. Yang, T. Yao, J. E. S. Szymanowski, J. Neuefeind, G. E. Sigmon, J. Lian, M. G. Tucker, B. D. Wirth, and M. Lang, Oxygen point defect accumulation in single-phase UO_{2+x}, Phys. Rev. Mater. **3**, 053611 (2019).

[39] R. I. Palomares, J. Shamblin, C. L. Tracy, J. Neuefeind, R. C. Ewing, C. Trautmann, and M. Lang, Defect accumulation in swift heavy ion-irradiated CeO_2 and ThO_2, J. Mater. Chem. A **5**, 12193 (2017).